

Supplemental Material for "Möbius strip microlasers: a testbed for non-Euclidean photonics."

Yalei Song,^{1,2} Yann Monceaux,¹ Stefan Bittner,³ Kimhong Chao,¹ Héctor M. Reynoso de la Cruz,^{1,4} Clément Lafargue,¹ Dominique Decanini,⁵ Barbara Dietz,² Joseph Zyss,¹ Alain Grigis,⁶ Xavier Checoury,⁵ and Mélanie Lebental¹

¹*Laboratoire Lumière, Matière et Interfaces (LuMin) CNRS, ENS Paris-Saclay, Université Paris-Saclay, CentraleSupélec, Gif-sur-Yvette, France.*

²*Lanzhou Center for Theoretical Physics and the Gansu Provincial Key Laboratory of Theoretical Physics, Lanzhou University, Lanzhou, 730000 Gansu, China.*

³*Chair in Photonics, LMOPS EA 4423 Laboratory, CentraleSupélec and Université de Lorraine, 2 rue Edouard Belin, 57070 Metz, France*

⁴*Science and Engineering Division of the University of Guanajuato, Department of Physical Engineering, Academic Body of Statistical Mechanics, León, Gto., México.*

⁵*Centre de Nanosciences et de Nanotechnologies, CNRS, Université Paris-Saclay, 10 Boulevard Thomas Gobert, Palaiseau, 91120, France.*

⁶*Laboratoire d'Analyse, Géométrie et Applications, CNRS UMR 7539, Université Sorbonne Paris Cité, Université Paris 13, Institut Galilée, 99 avenue Jean-Baptiste Clément, 93430 Villetaneuse, France*

(Dated: July 29, 2021)

This supplemental material first describes periodic orbits of the flat Möbius strip billiard. Then we present the algorithm which was implemented to find periodic geodesics for the Möbius strip. This algorithm can be used for smooth and differentiable surfaces. Furthermore periodic geodesics of the 3D Möbius strip are discussed in comparison with those of the flat Möbius billiard. We then present FDTD calculations of the resonant modes of the 3D Möbius strip and further examples of its modes. Finally the effective index approximation is derived for curved layers and additional experiments are shown.

The Möbius strip, parametrized by the set of Equations (1-3) in the main text, is hereafter referred to as *3D Möbius strip* to distinguish it from the *flat Möbius billiard*. Please note that all calculations presented in this Supplemental Material are made for a Möbius strip with chirality corresponding to an additional minus sign in Eq. (2) for the y coordinate.

I. THE FLAT MÖBIUS BILLIARD

In this section we discuss the flat Möbius billiard, which has fundamentally different ray dynamics compared to the three-dimensional (3D) Möbius strip considered in the main text. These differences are discussed at the end of this section, and the structure of the periodic geodesics of the 3D Möbius strip is compared to those of the flat Möbius billiard in Section III.

The flat Möbius billiard is defined as a rectangle with length $D = 2\pi R$ and width W where the transverse boundaries, defined by $x \in [0, D]$ at $y = \pm W/2$, are hard walls with specular reflections. The diagonally opposite corners are identified with each other, that is, periodic boundary conditions in longitudinal (x) direction with an inversion of the transverse (y) coordinate are imposed to obtain the topology of a Möbius strip, that is

$$\begin{aligned} x = D &\rightarrow x = 0 \\ y|_{x=0} &= -y|_{x=D} \\ \dot{y}|_{x=0} &= -\dot{y}|_{x=D} \end{aligned} \quad (\text{S1})$$

as illustrated in Fig. S1(a).

A. Periodic orbits of the flat Möbius billiard

The Periodic Orbits (POs) of the flat Möbius billiard are classified by the index pair (n_t, n_l) where n_t is the number of reflections at the transverse boundaries and n_l is the number of roundtrips in longitudinal (x) direction. Several examples are shown in Fig. S1. Since the transverse velocity component \dot{y} must return to its initial value after one roundtrip along a PO, and each reflection as well as each roundtrip in longitudinal direction change the sign of \dot{y} , the sum of n_t and n_l must be even. The only exception is the $(0, 1)$ periodic orbit (and its odd repetitions) because $\dot{y} = 0$ in this case [see Fig. S1(b)]. It is an isolated PO whereas all other POs are part of a family that covers the whole billiard.

The lengths of the POs are given by

$$L(n_t, n_l) = [(n_t W)^2 + (n_l D)^2]^{1/2} \quad (\text{S2})$$

and their momentum vectors $\vec{k} = (k_x, k_y)$ fulfill $|k_x| = k \cos(\alpha)$ and $|k_y| = k \sin(\alpha)$ with

$$\alpha(n_t, n_l) = \arctan[n_t W / (n_l D)]. \quad (\text{S3})$$

Any trajectory with a momentum vector fulfilling Eq. (S3) is a PO, independently of its initial position.

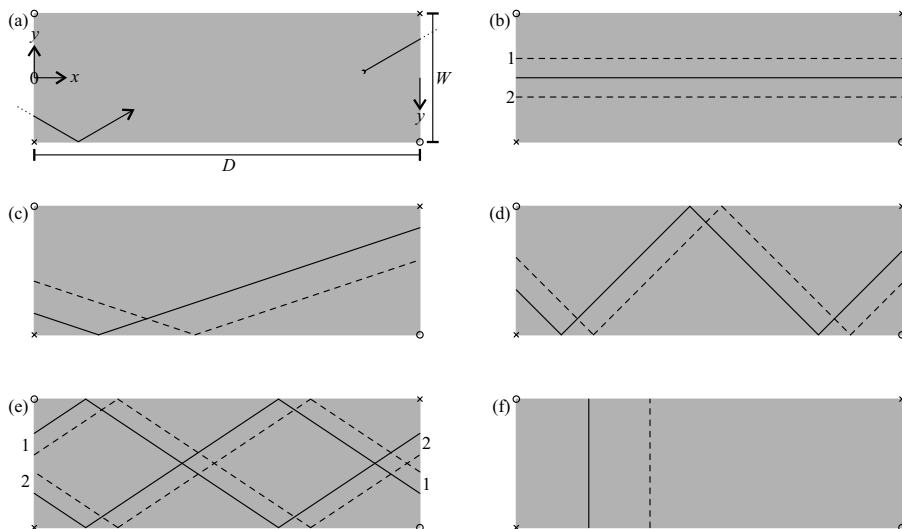


FIG. S1. Periodic orbits in the flat Möbius billiard. (a) Geometry of the flat Möbius billiard of length D and width W . The boundaries at $x = 0$ and $x = D$ are identified with each other after an inversion of the y direction, hence the points marked by o and x are identified with each other, respectively. (b) The isolated periodic orbit $(n_t, n_l) = (0, 1)$ (solid line) and one PO of the $(0, 2)$ family (dashed line). (c) Two examples of the $(1, 1)$ PO family. (d) Two examples of the $(3, 1)$ family. (e) Two examples of the $(4, 2)$ family. (f) Two examples of the $(2, 0)$ PO family, also called bouncing-ball orbits. The numbers 1 and 2 in panels (b) and (e) indicate the connections of the different PO segments.

B. Developable and non-developable surfaces

The flat Möbius billiard is a representation of a developable Möbius strip. Developable surfaces are smooth surfaces with vanishing Gaussian curvature [1], where the Gaussian curvature is the product of the two principal curvatures at a given point. Developable surfaces have a flat metric like the Euclidean plane, that is, there exists a parametrization of the surface such that the metric tensor is $g_{ij} = \delta_{ij}$. Developable surfaces can be obtained by rolling a piece of paper without stretching, compression, folding or similar distortions. A cylinder is an example of a developable surface, but also a Möbius created from a paper strip. Since the geodesics of a surface only depend on its metric, the flat Möbius billiard considered above is equivalent to any developable Möbius strip (like the one in Ref. [2]) as far as their ray dynamics is concerned.

Non-developable surfaces, on the other hand, have a non-vanishing Gaussian curvature and a metric that is not flat. This is the case for the 3D Möbius strip considered here. The differences in the structure of the periodic geodesics and the ray dynamics in general between the flat Möbius billiard and the 3D Möbius strip originate from the fact that the former is developable and the latter not. Generally speaking, the ray dynamics on a curved surface is not necessarily different from that of a flat billiard, only a non-vanishing Gaussian curvature will lead to a real difference. Hence non-developable surfaces are of greater interest and more likely to exhibit novel effects.

II. CALCULATION OF GEODESICS

A. Local approach

A curve $\gamma(s)$ parametrized by s on a curved surface along $\vec{r} = \vec{r}[q_1(s), q_2(s)]$ is a geodesic if it fulfills

$$\frac{d^2 q^k}{ds^2} + \sum_{i,j} \Gamma_{ij}^k \frac{dq^i}{ds} \frac{dq^j}{ds} = 0 \quad (\text{S4})$$

with $i, j, k = 1, 2$ (see Eq. 7.19b in Ref. [3]). The Christoffel symbols are given by

$$\Gamma_{ij}^k = \frac{1}{2} \sum_m g^{km} \left(\frac{\partial g_{mi}}{\partial q^j} + \frac{\partial g_{mj}}{\partial q^i} - \frac{\partial g_{ij}}{\partial q^m} \right) \quad (\text{S5})$$

where (g_{ij}) is the metric tensor and (g^{ij}) its inverse. For the 3D Möbius strip

$$g_{11} = R^2 + \frac{q_2^2}{4} [3 + 2 \cos(q_1)] + 2Rq_2 \cos\left(\frac{q_1}{2}\right) \quad (\text{S6})$$

with the coordinates $q = (q_1, q_2)$ parametrizing the surface of a 3D Möbius strip as defined in the main text. The other tensor elements are $g_{22} = 1$ and $g_{12} = g_{21} = 0$.

The element g_{11} is shown as function of (q_1, q_2) in Fig. S2. Since g_{11} is not constant, the 3D Möbius strip is non-developable, and the Gaussian curvature of the Möbius strip varies locally. This has important consequences for the structure of the periodic geodesics as compared to the flat Möbius billiard as explained in Section III.

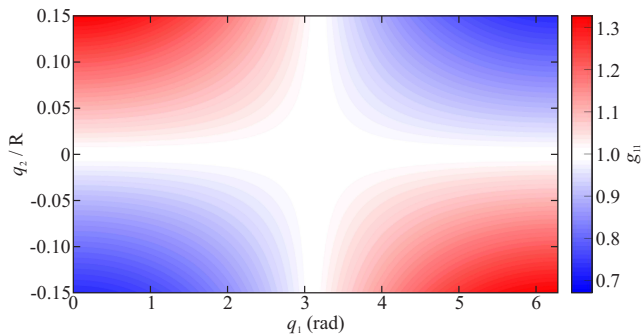


FIG. S2. Metric tensor element g_{11} for the 3D Möbius strip as function of the generalized coordinates $q = (q_1, q_2)$.

Solving this initial conditions problem for finding the periodic geodesics evidently requires knowledge of the initial values of $q(s)$ and of $\dot{q}(s) = dq(s)/ds$. For the Möbius strip, Eqs. (S4) must be solved numerically with an algorithm such as the fourth-order Runge-Kutta method.

Finding periodic geodesics by solving an initial conditions problem is difficult since it is *a priori* unknown which initial position and velocity lead to a periodic trajectory. Hence, a large parameter space needs to be explored with high resolution. Moreover, it is difficult to judge whether a numerical solution of these equations is indeed a periodic geodesic, in view of the unavoidable numerical inaccuracies. A variational approach is simpler and more efficient.

B. Variational approach

Since a geodesic is the locally shortest path between two points — which is essentially Fermat's principle — we can find a geodesic segment connecting two points with coordinates $Q^{(0)} = q(0)$ and $Q^{(1)} = q(1)$ by searching the trajectory $\gamma(s)$ for which the length L_γ given by

$$L_\gamma = \int_0^1 ds \left[\sum_{i,j} g_{ij}[q(s)] \frac{dq_i}{ds}(s) \frac{dq_j}{ds}(s) \right]^{1/2} \quad (\text{S7})$$

is stationary. This formulation as a boundary condition problem no longer requires *a priori* knowledge of the initial velocity \dot{q} . However, the two vertices $Q^{(0,1)}$ must be given beforehand and are fixed. Constructing a periodic geodesic requires calculating several such segments that are connected in a closed loop with vertices on the boundary of the Möbius strip. Then all the vertices, including the initially fixed vertices $Q^{(0,1)}$, are varied. This will be described in more detail in the following.

We start with the algorithm to calculate a single geodesic segment. Since it is not possible to solve analytically this infinitely-dimensional variational problem for the 3D Möbius strip, we tackle it numerically using a discretized trajectory $\gamma = \{q(n)\}$ with $n = 1 \dots N$ where

$q(1)$ corresponds to $Q^{(0)}$ and $q(N)$ to $Q^{(1)}$. The integral for L_γ is then approximated by a sum over the N discretization points using the trapezoidal rule where the derivatives of $q(s)$ in Eq. (S7) are replaced by central finite differences. The trajectory γ is stationary when all the derivatives $\partial L_\gamma / \partial q_i(n)$ vanish. Here, variation is performed perpendicular to the curve $\gamma(s)$. For this, the derivative $v_n = \partial L_\gamma / \partial q_\perp(n)$ is computed in the direction $q_\perp(n)$ which is perpendicular to the trajectory in q space at discretization point n , implying that the two coordinates $[q_1(n), q_2(n)]$ at discretization point n are not varied independently. Note that a variation tangential to the trajectory would correspond to a perturbation along the trajectory which implies a change in s . Therefore, as is general practice, we do not consider this variation.

The trajectory segment is initialized with a straight line in q space. The correct solution for which \vec{v} vanishes is found using a Newton iteration, that is, $q(n) \rightarrow q(n) - d_n q_\perp(n)$ where \vec{d} — a N component vector — is the solution of $H\vec{d} = \vec{v}$. The matrix elements of H are

$$H_{mn} = \frac{\partial^2 L_\gamma}{\partial q_\perp(m) \partial q_\perp(n)}, \quad (\text{S8})$$

so \vec{v} and H are the first and second derivatives (gradient and Hessian), respectively, of L_γ with respect to the $q_\perp(n)$. Since the first and last point of the segment are kept fixed, only the elements with indices in the range $2 \dots N - 1$ of vectors \vec{v} and \vec{d} and matrix H are considered in the above equations. The Newton iteration is continued till \vec{v} converges to $\vec{0}$ within machine precision.

In order to find a periodic geodesic consisting of M segments, $M + 1$ vertices $Q^{(m)}$ on the boundary of the Möbius strip are chosen with values $Q_2^{(m)} = \pm W/2$ selected according to a symbolic code (see below) and the $Q_1^{(m)}$ chosen randomly in ascending order. In a first step, the M individual segments are iterated as described above to find the geodesics connecting the different vertices which are kept fixed. In a second step, one step of the Newton iteration for all discretization points including all of the vertices $Q^{(m)}$ is calculated, where the vertices are only allowed to vary in the q_1 direction to keep them on the boundary of the Möbius strip. Steps one and two are repeated till the trajectory becomes stationary within machine precision. To ensure periodicity, $Q^{(0)}$ and $Q^{(M)}$ are initialized such that they represent the same point in configuration space, that is, $Q_1^{(M)} = Q_1^{(0)} + 2\pi n_l$ and $Q_2^{(M)} = (-1)^{n_l} Q_2^{(0)}$ where n_l is the number of revolutions around the Möbius strip, and the same variation is applied to both of them.

A large number of random initial conditions for the vertices $Q^{(m)}$ was tested for each considered symbolic code since the algorithm only converges to a physical trajectory if the initial conditions are sufficiently close to a correct solution. A vanishing gradient \vec{v} proves that the calculated trajectories are numerically exact geodesics. Typically, 10,000 discretization points per revolution were used in the calculations, and it was checked that

increasing the number of discretization points did not significantly change the length L_γ or the shape of the trajectory.

Furthermore, it was verified that the law of elastic reflection is respected at all vertices, i.e., that the ingoing angle is equal to the outgoing angle. It should be noted that the law of elastic reflection is not *a priori* assumed in any way during the numerical calculations of the periodic geodesics but results when a correct solution is found. In addition, several periodic geodesics were verified independently by solving the equations (S4) with the correct initial conditions.

III. PERIODIC GEODESICS OF THE 3D MÖBIUS STRIP

In this Section, additional examples of periodic geodesics of the 3D Möbius strip are shown and their structure is compared to the periodic orbits in the flat Möbius billiard and conventional ring cavities.

Figure S3 shows three typical examples. Some periodic geodesics like those in Figs. S3(a-d) are symmetric with respect to a rotation of 180° around the x -axis, which is the symmetry axis of the Möbius strip and indicated as green dashed line in the configuration space plots. These trajectories all pass through the point $q = (\pi, 0)$ indicated as green dot in the q space plots. Other orbits such as the one shown in Figs. S3(e, f) are not, and they transform to a distinct periodic geodesic under the symmetry rotation by 180° .

The periodic geodesics are labeled by indices (n_t, n_l) and a symbolic code, where n_t is the number of vertices at the boundary and n_l is the number of revolutions around the Möbius strip. The symbolic code consists of n_t letters that connect vertices with a different or same sign of q_2 , i.e., reflection points on Opposite boundaries or the Same boundary, though the notion of "same" and "opposite" side only makes sense from a local perspective given that the Möbius strip actually has only one boundary¹. The $(11, 1, o^{11})$ orbit in Figs. 2(c, e) of the main text, for example, has a zig-zag structure where all segments connect opposite sides, whereas the $(5, 1, s^2os^2)$ orbit in Figs. 2(d, f) of the main text starts with two segments connecting the same side, followed by a segment connecting to the opposite side after half a round trip followed by two segments connecting the same side again.

The existence of specific periodic geodesics depends on the aspect ratio W/R . For example, the $(5, 1, so^3s)$ geodesic in Figs. S3(e, f) does not exist for smaller aspect ratios such as $W/R = 0.3$. As the aspect ratio is decreased and the strip becomes narrower, the segment connecting vertices 1 and 2 eventually touches the lower

boundary $q_2 = -W/2$ and the geodesic hence ceases to exist. In contrast, the periodic orbits of the flat Möbius billiard exist independently of its aspect ratio.

The three periodic geodesics in Fig. S3 all have structures that cannot be found for periodic orbits of the flat Möbius billiard. First, all of them feature segments that connect to the same boundary (code s), however such segments are impossible in the flat Möbius billiard. Furthermore, some periodic geodesics such as the $(4, 1, sos^2)$ in Figs. S3(c, d) have $n_t + n_l$ odd, whereas it must always be even for the flat Möbius. First, these differences can be directly attributed to the fact that the 3D Möbius strip is non-developable and thus has a non-vanishing Gaussian curvature, implying that some parts of the boundary are convex and thus permit s trajectory segments, whereas the straight boundary of the flat Möbius billiard does not allow them. Second, $n_t + n_l$ must be even in the flat Möbius since \dot{y} can only change its sign at a reflection but stays constant in between, whereas \dot{q}_2 changes continuously during the propagation on the curved surface of the 3D Möbius strip in addition to the sign changes at the vertices.

Another difference is that the POs of the flat Möbius billiard are all part of a continuous family whereas the periodic geodesics of the 3D Möbius strip are all isolated, with one exception given below. The existence of families of POs is due to the continuous translational symmetry in x direction of the flat Möbius billiard. While the 3D Möbius strip has a similar periodic boundary condition as the flat Möbius billiard, the metric tensor g_{ij} does not exhibit a continuous translational symmetry, see Fig. S2. The periodic geodesics are isolated due to this reduction of symmetry.

There is one series of periodic geodesics, the $(n_t, 1, o^{n_t})$ orbits with n_t odd, that resembles the $(n_t, 1)$ periodic orbits of the flat Möbius billiard. Three examples of such periodic geodesics are shown as red lines in Fig. S4. The analog POs of the flat Möbius billiard are indicated as blue dashed lines, where the coordinate x (y) of the flat Möbius billiard is identified with q_1 (q_2). As the number of reflections n_t increases, the segments of the periodic geodesics become less and less curved in q space and increasingly resemble the straight segments of the POs of the flat Möbius billiard, where the segments in the region around $q_1 = 0, 2\pi$ exhibit generally more curvature than those in the region around $q_1 = \pi$. Also the lengths of the periodic geodesics become closer to the lengths of the corresponding POs in the flat Möbius.

While the $(n_t, 1, o^{n_t})$ periodic geodesics slowly converge towards the corresponding POs of the flat Möbius billiard for increasing n_t , some differences remain. First, these periodic geodesics only exist for $n_t \geq 9$ for the aspect ratio $W/R = 0.375$ considered here ($n_t \geq 11$ for $W/R = 0.3$) because the concave parts of the boundary do not allow some of the longer segments needed for smaller n_t . Second, the periodic geodesics remain isolated since the 3D Möbius strip lacks the translational symmetry of its flat counterpart.

¹ The labels are not unambiguous since several distinct periodic geodesics with the same indices and code can exist.

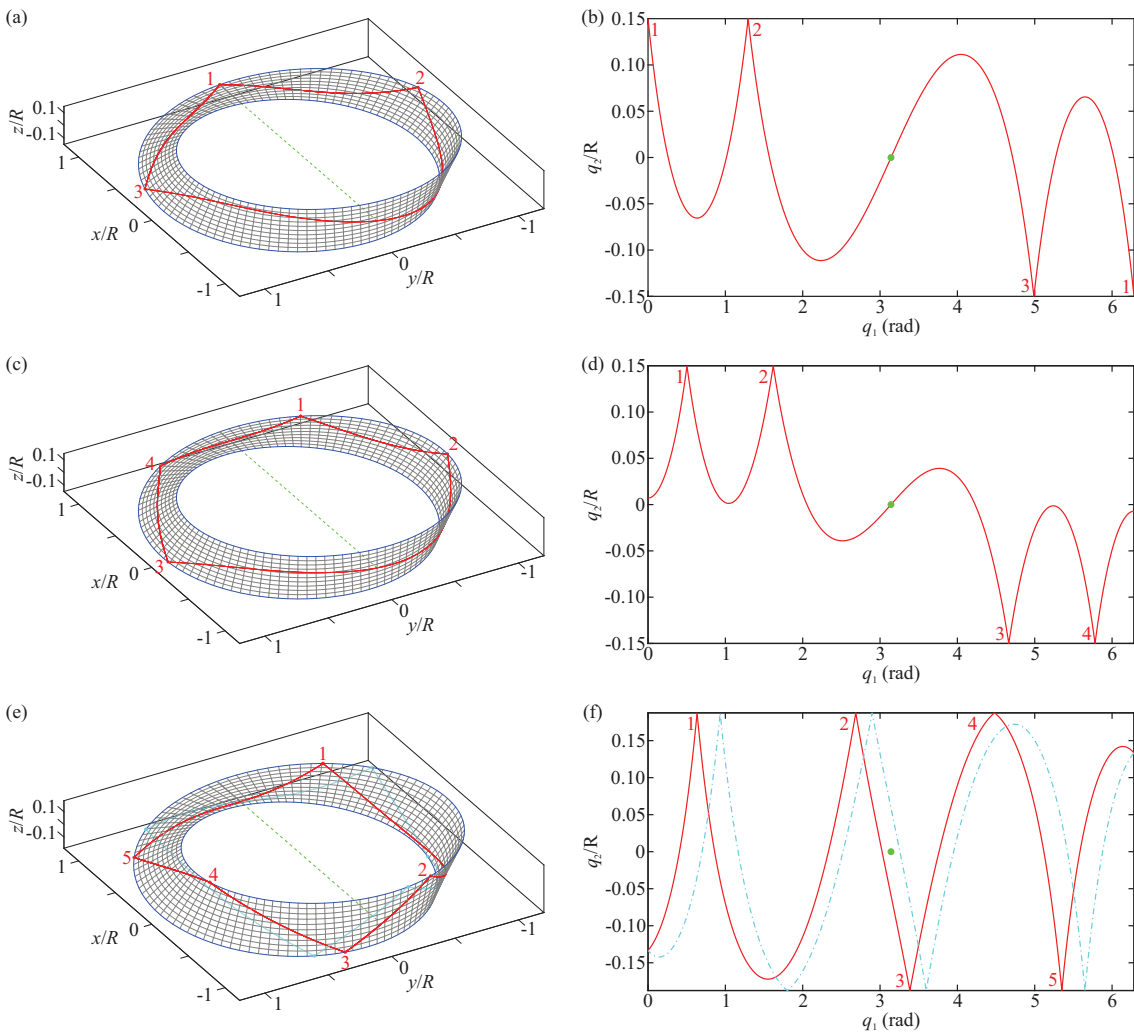


FIG. S3. Further examples of periodic geodesics (red solid lines) in configuration (a, c, e) and q space (b, d, f). The green dots and the dashed green line indicates the symmetry axis. (a, b) Periodic geodesic $(3, 1, sos)$ with length $L = 6.53R$ on a Möbius strip with aspect ratio $W/R = 0.3$. (c, d) Periodic geodesic $(4, 1, sos^2)$, called 4a in the following, with length $L = 6.66R$ on a Möbius strip with $W/R = 0.3$. (e, f) Periodic geodesic $(5, 1, so^3s)$ with length $L = 6.67R$ on a Möbius strip with $W/R = 0.375$. Its symmetry partner obtained by rotation around the x -axis (green dashed line) is indicated as cyan dash-dotted line.

These two effects can be understood by considering the metric tensor. For the flat Möbius billiard, $g_{ij} = \delta_{ij}$, and hence all geodesics are straight lines. For the 3D Möbius strip, $g_{22} = 1$ as well, but g_{11} deviates from unity (see Fig. S2) implying that the geodesics are curved in q space. However, the more the velocity vector \dot{q} of a trajectory becomes parallel to the q_2 direction and thus \dot{q}_1 decreases, which is necessarily the case when n_t increases, the less important the contribution of g_{11} is, which results in less curvature. Therefore, the segments of the periodic geodesics resemble more and more straight lines as n_t increases. Moreover, the deviation of g_{11} from 1 is smallest in the region around $q_1 = \pi$, and hence the trajectory segments are less curved there.

A special case are the $(2, 0, o^2)$ geodesics that bounce back and forth perpendicularly between the sides of the

Möbius strip, in analogy to the bouncing-ball orbits of the flat Möbius billiard shown in Fig. S1(f). They are the only periodic geodesics that form a continuous family, that is, any trajectory with $q_1 = \text{const.}$ belongs to this family. Since $\dot{q}_1 = 0$, the spatially varying tensor element g_{11} has no effects for these geodesics, whereas $g_{22} = 1$ is homogeneous. Thus, these periodic geodesics have the same properties as their counterparts in the flat Möbius billiard.

While the flat Möbius billiard features POs without reflections at the boundaries, i.e., the $(0, n_l)$ orbits in Fig. S1(b), such periodic geodesics were not found for the 3D Möbius strip. In particular, trajectories with $q_2 = \text{const.}$ such as the one shown in Fig. 2(a) of the main text are not geodesics since $g_{11} \neq 1$, and hence $\dot{q}_2 \neq 0$ for almost all points of a geodesic. Therefore, at least

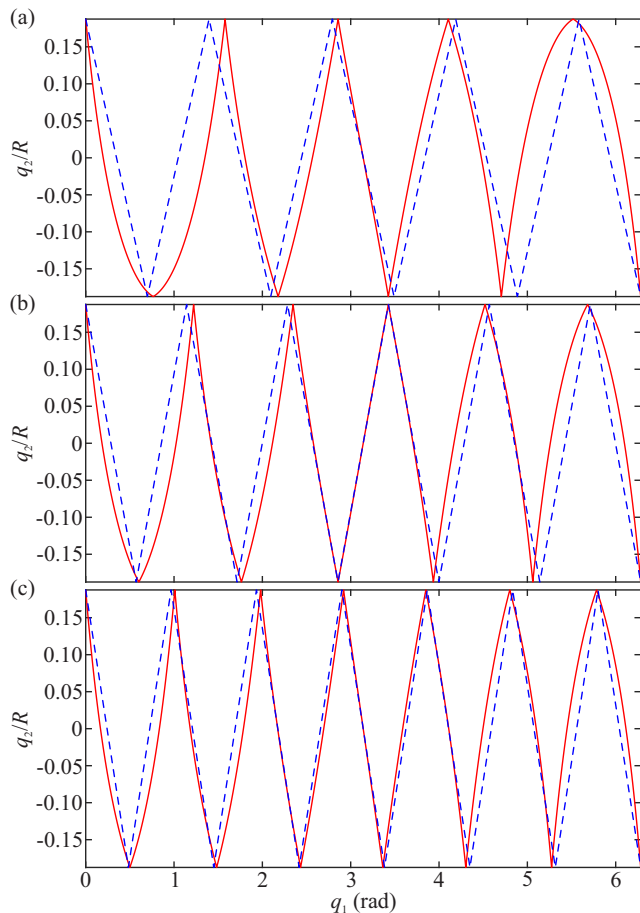


FIG. S4. Periodic geodesics of $(n_t, 1, o^{n_t})$ type (red solid lines) on a 3D Möbius strip with aspect ratio $W/R = 0.375$. They resemble the $(n_t, 1)$ periodic orbits of the flat Möbius billiard which are indicated as blue dashed lines. (a) Geodesic $(9, 1, o^9)$ with length $L = 7.03R$. The length of the $(9, 1)$ PO is $7.13R$. (b) Geodesic $(11, 1, o^{11})$ with length $L = 7.44R$. The length of the $(11, 1)$ PO is $7.52R$. (c) Geodesic $(13, 1, o^{13})$ with length $L = 7.89R$. The length of the $(13, 1)$ PO is $7.95R$.

one reflection at the boundary is needed to compensate the change of sign of \dot{q}_2 after one round trip due to the periodic boundary conditions with inversion of q_2 .

It is also interesting to compare the Möbius strip with conventional whispering gallery resonators exhibiting azimuthal rotational symmetry such as rings, spheres or toroids. Such resonators are of interest since they feature modes with ultra-high quality (Q) factors due to the existence of whispering gallery trajectories that propagate along the outer resonator wall with a constant angle of incidence above the critical angle for total internal reflection. High- Q modes exist even for small deformations of the rotational symmetry that break angular momentum conservation.

Evidently, the 3D Möbius strip does not have an azimuthal symmetry that would preserve the angular momentum. More importantly, whispering gallery type tra-

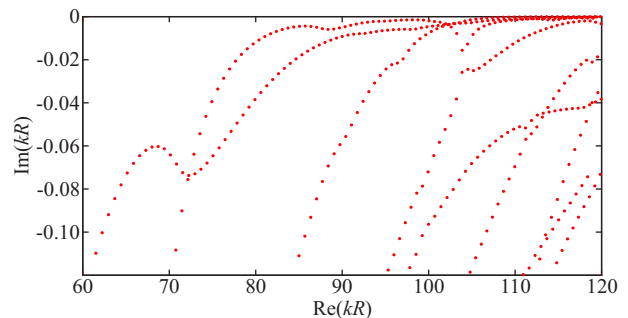


FIG. S5. Real versus imaginary parts of the eigenwavenumbers (i.e. spectrum) calculated with 3D FDTD simulations for a Möbius strip with $R = 10 \mu\text{m}$, $W = 3 \mu\text{m}$, $h = 150 \text{ nm}$, and $n = 1.515$. Only the modes symmetric with respect to the x -axis are shown.

jectories, which would have a symbolic code s^{nt} , cannot exist since parts of the boundary are concave and thus locally prohibit s -type segments. Moreover, the boundary of the Möbius strip is not a geodesic itself. Hence, all periodic geodesics must feature at least one o -segment that crosses the strip. In many cases an o -segment passing through or near the symmetry point $q = (\pi, 0)$ is found. As a consequence, the 3D Möbius strip cannot support whispering gallery modes, and the intensity distributions of its resonant modes typically show the same crossing behavior [see Fig. 6(d) in the main text and Figs. S6(d) and S7(d) below]. Nonetheless, resonances with high quality factors exist since many periodic geodesics such as the ones shown above are confined by total internal reflection at all reflections.

IV. 3D FDTD SIMULATIONS

In order to better understand the relation between the geodesics and the resonant modes of the Möbius strip, the spectrum as well as the field distributions of several modes are calculated for a Möbius strip with $R = 10 \mu\text{m}$, $W = 3 \mu\text{m}$, $h = 150 \text{ nm}$, and $n = 1.515$. Two examples of mode patterns are presented here in addition to the one shown in Fig. 6 of the main text. The calculation of the length spectrum is explained as well.

A. Spectrum of the Möbius strip

To obtain the spectrum of a Möbius strip, a 3D Finite Difference Time Domain (FDTD) simulation is performed with a temporally short (spectrally broad) excitation. The time evolution of the field at one point in the Möbius strip is recorded. To get an accurate estimate of the frequencies and lifetimes from the recorded time data, a spectral estimation technique known as Prony's method is used [4]. The calculated spectrum in Fig. S5 features several series of roughly equidistant resonant modes.

Since the Möbius strip exhibits a two-fold rotation symmetry with respect to the x -axis (C_2 symmetry), its modes are either symmetric or antisymmetric with respect to this rotation. The spectrum with symmetric modes in Fig. S5 is calculated using an excitation dipole in the middle of the flat part of the strip at $(R, 0, 0)$ with electric field parallel to the x -axis. Antisymmetric modes (not shown) are calculated as well by displacing the excitation dipole away from the symmetry axis. The symmetric and antisymmetric modes are almost degenerate, with a relative deviation of typically $2 \cdot 10^{-2}$ in $\text{Im}(kR)$ and an even smaller relative deviation of about $2 \cdot 10^{-7}$ in $\text{Re}(kR)$. It should be noted that a C_2 symmetry does not imply degeneracies.

In addition we performed simulations with posts which were positioned as in the experiments. The resulting series of modes barely differed from those obtained with no posts. However, the losses slightly increased because a small fraction of modes propagating within the Möbius strip was scattered out by the posts. In summary, the posts do not significantly impact the structure of the spectrum and hence our conclusions about the relation to periodic geodesics remain valid.

B. Mode patterns and geodesics

To calculate the field distribution of a particular resonance, a narrow band excitation at the targeted frequency is used so that only the targeted mode is excited in the FDTD simulation. Two examples in addition to Fig. 6 in the main text are shown in Figs. S6 and S7. In contrast to the mode shown in Fig. 6, which exhibits only a single transverse excitation, the modes in Figs. S6 and S7 have a second-order transverse excitation. The three modes belong to different branches of the spectrum, respectively.

The mode in Fig. S6 shows good agreement with a periodic geodesic of type $(4, 1, sos^2)$, geodesic 4a shown in Fig. S3(c, d). The agreement of the mode in Fig. S7 with geodesic $(6, 1, s^2os^3)$ is excellent. These examples confirm that some modes of the Möbius strip are closely related to periodic geodesics of various types, though not all modes show a clear connection to a single periodic geodesic. It furthermore appears that better agreement is found for modes with higher excitation frequency $\text{Re}(kR)$, that is, in the semiclassical limit.

C. Length spectrum

Figure 5 of the main text shows the Fourier transform of the numerically calculated spectrum (cf. Fig. S5). It is referred to as *length spectrum* since it peaks at the lengths of the underlying periodic orbits or geodesics. Since the effective refractive index of the simulated Möbius strip varies significantly as function of frequency between $n_{\text{eff}} \simeq 1.12$ and 1.27 in the range of $\text{Re}(kR) = 60$ – 120 ,

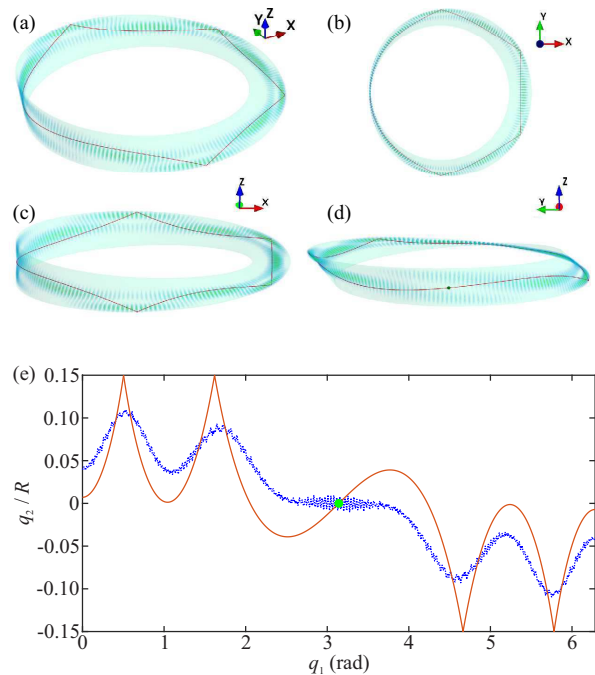


FIG. S6. (a)-(d) Different views of the same mode with $\text{Re}(kR) = 77.843$ and $\text{Im}(kR) = -0.0494$ ($Q = 788$). $|\vec{E}|^2$ is shown in false colors. A geodesic of type $(4, 1, sos^2)$ with length $6.656R$ is superimposed as red lines. The green dot in panel (d) indicates the intersection of the x -axis with the vertical section of the Möbius strip. (e) Representation of the geodesic (red solid line) as function of $q_{1,2}$. The blue dotted line is the mean position of the mode calculated from Eq. (9) in the main text. The green dot indicates the symmetry axis.

the Fourier transform is slightly modified in order to account for this dispersion. Following Ref. [5], the Fourier transform is calculated as

$$\hat{\rho}(\ell) = \sum_j \exp\{-ik_j \ell n_{\text{eff}}[\text{Re}(k_j)]\} \quad (\text{S9})$$

where the k_j are the eigenwavenumbers of the resonances and the refractive index in the exponential was replaced by the effective refractive index at the respective resonance frequency. A total of 628 symmetric modes in the range of $60 \leq \text{Re}(kR) \leq 120$ and with $\text{Im}(kR) \geq -0.60$ were used in the calculation. Figure 5 shows $|\hat{\rho}|$ as function of the geometric length ℓ .

V. EFFECTIVE REFRACTIVE INDEX

The effective index approximation assumes that the 3D (scalar) Helmholtz equation

$$(\Delta + n^2 k^2) \psi = 0 \quad (\text{S10})$$

can be approximated by the 2D Helmholtz equation

$$\Delta_s \psi_s + n_{\text{eff}}^2 k^2 \psi_s = 0 \quad (\text{S11})$$

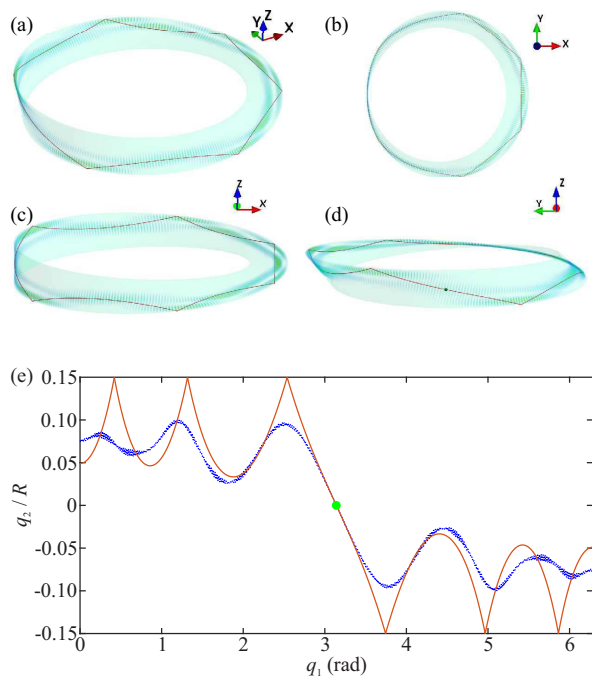


FIG. S7. (a)-(d) Different views of the same mode with $\text{Re}(kR) = 109.260$ and $\text{Im}(kR) = -0.00021$ ($Q = 265, 370$). $|\vec{E}|^2$ is shown in false colors. A geodesic of type $(6, 1, s^2os^3)$ with length $6.779R$ is superimposed as red lines. The green dot in panel (d) indicates the intersection of the x -axis with the vertical section of the Möbius strip. (e) Representation of the geodesic (red solid line) as function of $q_{1,2}$. The blue dotted line is the mean position of the mode calculated from Eq. (9) in the main text. The green dot indicates the symmetry axis.

where Δ_s is the Laplace operator on the curved surface and $\psi_s(q_1, q_2)$ the wave function on the surface. Then the effective index n_{eff} includes the influence of the finite thickness of the resonator in the q_3 direction perpendicular to the surface.

This Section deals with two issues. In Section V A, we derive the effective index for a curved layer and show that, for the range of parameters considered in experiments, there is no difference with a flat layer. In Section V B, we investigate the experimental value of the group refractive index n_g and its uncertainty, which yields the value $n_g = 1.58 \pm 0.05$.

A. Derivation

The effective index approximation is usually computed for flat layers. However, in the (q_1, q_3) plane, a section of the Möbius strip locally looks like a ring, with a local radius of curvature varying from R to ∞ (i.e., a flat layer). Following Ref. [6], we extend the derivation of the effective index approximation to a curved layer, which is assumed to be a segment of a ring of inner radius a and outer radius b . In correspondence with experiments, we

use $b = 50 \mu\text{m}$, $b - a = 1 \mu\text{m}$, and a bulk refractive index $n = 1.515$ for the photoresist [7].

First the eigenfunctions ϕ of the ring are calculated based on the ansatz

$$\begin{aligned} r < a & : \phi(r, \theta) = AJ_m(kr)e^{im\theta} \\ a < r < b & : \phi(r, \theta) = J_m(nkr)e^{im\theta} + BY_m(nkr)e^{im\theta} \\ b < r & : \phi(r, \theta) = CH_m^{(1)}(kr)e^{im\theta} \end{aligned} \quad (\text{S12})$$

where J_m and Y_m are the Bessel functions of the first and second kind, respectively, $H_m^{(1)}$ is the Hankel function of the first kind, their order m is an integer. A , B , and C are constants, and r , θ are the standard circular coordinates. We consider the polarization of the electric field to be parallel to the layer. Applying the continuity conditions at the boundaries $r = a$ and $r = b$, we get

$$\begin{aligned} \frac{J'_m(ka)}{J_m(ka)} J_m(nka) - nJ'_m(nka) &= \\ nY'_m(nka) - Y_m(nka) \frac{J'_m(ka)}{J_m(ka)} &= \\ \frac{H'_m(kb)}{H_m(kb)} J_m(nkb) - nJ'_m(nkb) &= \\ nY'_m(nkb) - Y_m(nkb) \frac{H'_m(kb)}{H_m(kb)} & \end{aligned} \quad (\text{S13})$$

where the prime denotes the derivative. For each value of m , there are several eigenwavenumbers k which correspond to different excitations in the direction q_3 . The effective index is defined via

$$m = n_{\text{eff}}kr_0 \quad (\text{S14})$$

where r_0 is the radial center of mass of the wave function in the ring. In the frequency range corresponding to the experiments, the wave functions are well centered in the ring, so we assume r_0 in the middle, $r_0 = (a + b)/2$. We calculate the k eigenwavenumbers for various m values based on Eq. (S13) and then plot

$$n_{\text{eff}} = \frac{m}{kr_0}. \quad (\text{S15})$$

Figure S8 shows the comparison of the effective index for a flat and a curved layer in the range of k corresponding to the experiments. The effective indices for flat and curved layers agree excellently for the parameter range considered here, that is, the curvature causes a negligible change of n_{eff} compared to the flat case even for the smallest radius of curvature, $50 \mu\text{m}$, found in the Möbius strip. Consequently we can assume that the effective index is constant throughout the Möbius strip (i.e., independent of the local curvature) and equal to that of a flat layer with the same thickness.

B. Experiments

As discussed in the main text, the Fourier transform of the laser spectrum exhibits peaks at the optical length(s)

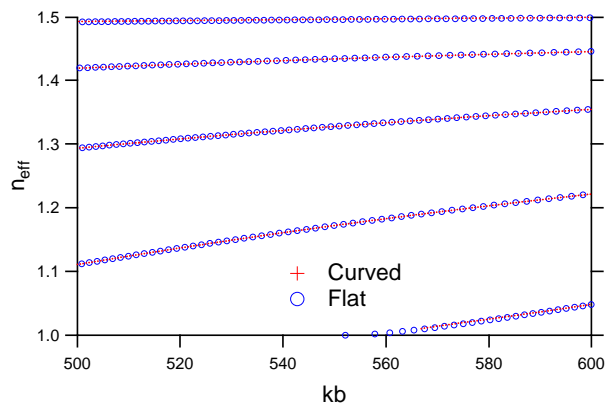


FIG. S8. Effective refractive index for a flat layer [Eq. (4) in [8]] and a curved layer for $n = 1.515$, an outer radius $b = 50 \mu\text{m}$, and an inner radius $a = 49 \mu\text{m}$ in the experimental wavelength range $\lambda = 2\pi/k = 560 \text{ nm}$ to $\lambda = 600 \text{ nm}$. The electric field is assumed parallel to the layer.

of the underlying periodic orbit(s). The geometrical length of these trajectories is obtained by dividing by the group refractive index (see Ref. [9]). It is the sum of the effective index and contributions from the material dispersion of the bulk index n and modal dispersion due to n_{eff} approximation,

$$n_g = n_{\text{eff}} + k \left. \frac{\partial n}{\partial k} \right|_{\text{mat}} + k \left. \frac{\partial n}{\partial k} \right|_{\text{eff}}. \quad (\text{S16})$$

The bulk refractive index is $n = 1.515 \pm 0.005$ [7]. Its dispersion is very small, thus we assume that n is constant when calculating n_{eff} . However, k is large, hence the term $k \left. \frac{\partial n}{\partial k} \right|_{\text{mat}}$ cannot be neglected. Following Ref. [9], it is inferred from the laser spectra of cuboids since their lasing modes are located on a well-known periodic orbit in the bulk of the cavity. From these data we estimate the material dispersion as $k \left. \frac{\partial n}{\partial k} \right|_{\text{mat}} = 0.05 \pm 0.04$.

The effective index and its dispersion are calculated as discussed in the previous section. In the frequency range of interest and for a $1 \mu\text{m}$ thick strip, there are four to five branches (excitations in the q_3 direction) for each polarization with significantly different indices and dispersion values. Since the spectrum in Fig. 3(a) exhibits a single series of resonances, we consider only the branch with the highest effective index which has the best confinement factor and thus the highest laser gain. The corresponding effective index is $n_{\text{eff}} = 1.49$ and its dispersion equals $k \left. \frac{\partial n}{\partial k} \right|_{\text{eff}} = 0.037 \pm 0.002$. Finally, adding the three terms in Eq. (S16) yields a group index of $n_g = 1.58 \pm 0.05$.

VI. ADDITIONAL EXPERIMENTS

A. Photographs

Figure S9 shows a lasing Möbius strip cavity registered with a Ueye camera equipped by a zoom Navitar. The

horizontal section of the Möbius surface is on the left and the vertical section on the right. Since the photoresist is transparent, only the edges of the Möbius strip as well as the pylons are seen as dark lines in the photographs

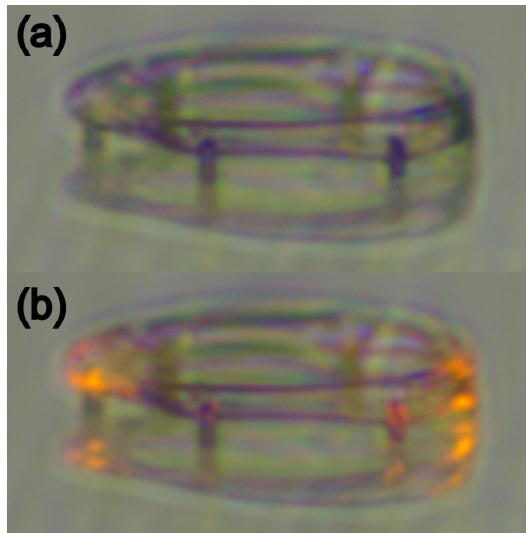


FIG. S9. Photographs of a Möbius strip illuminated with low intensity white light (a) without pump laser and (b) with pump. We can see the cavity and its reflection on the glass substrate. The resist IP-G780 is transparent. The green pump light is removed by a notch filter, while the laser emission is yellow.

B. Influence of the strip thickness

Experiments were performed with Möbius strip micro-lasers of thickness $h = 1, 2, 3,$ and $5 \mu\text{m}$, where $R = 50 \mu\text{m}$ and $W = 15 \mu\text{m}$. For $h = 1 \mu\text{m}$, the spectrum features a single series of resonances, independent of the pump intensity as shown in Fig. S10(a). For $h = 3 \mu\text{m}$ the spectrum exhibits a single series just above threshold, but becomes more complex as the pump intensity increases [see Fig. S10(b)]. However, its Fourier transform is peaked at the same optical length independently of the pump intensity. For $h = 5 \mu\text{m}$ thickness, in contrast, the spectrum and its Fourier transform are more complex, which means that the analysis using the effective index approximation is probably not valid. In Fig. 4 of the main text, only cavities with $h = 1 \mu\text{m}$ are considered to ensure that the effective index approximation remains valid.

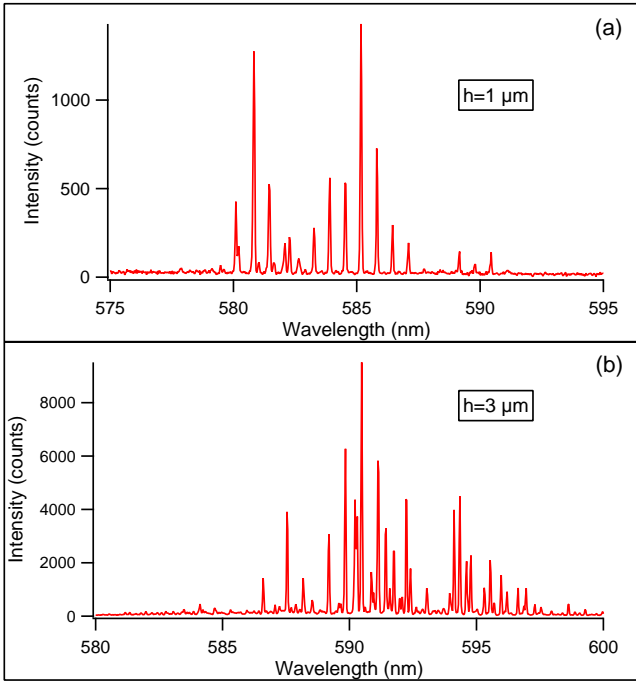


FIG. S10. Experimental spectra of Möbius strip microlasers for $R = 50 \mu\text{m}$ and $W = 15 \mu\text{m}$ with (a) $h = 1 \mu\text{m}$, and (b) $h = 3 \mu\text{m}$. All experimental parameters are identical for (a) and (b), in particular the pump intensity, which is four times the laser threshold of the microcavity in (a).

-
- [1] W. Kühnel, *Differential geometry. Curves — surfaces — manifolds*, Third edition, American Mathematical Society (2015).
- [2] J. Gravesen and M. Willatzen, *Eigenstates of Möbius nanostructures including curvature effects*, Phys. Rev. A **72**, 032108 (2005).
- [3] M. Nakahara, *Geometry, topology and Physics*, Second edition, Taylor and Francis (2003).
- [4] S. Lawrence Marple, Jr., *Digital Spectral Analysis*, Second edition, Courier Dover Publications (2019).
- [5] S. Bittner, E. Bogomolny, B. Dietz, M. Miski-Oglu, and A. Richter, *Application of a trace formula to the spectra of flat three-dimensional dielectric resonators*, Phys. Rev. E **85**, 026203 (2012).
- [6] R. S. Elliott, *Azimuthal surface waves on circular cylinders*, J. App. Phys. **26**, 368 (1955).
- [7] T. Gissibl, S. Wagner, J. Sykora, M. Schmid, and H. Giessen, *Refractive index measurements of photoresists for three-dimensional direct laser writing*, Optical Materials Express **7**, 2293 (2017).
- [8] M. Lebental, N. Djellali, C. Arnaud, J.-S. Lauret, J. Zyss, R. Dubertrand, C. Schmit, E. Bogomolny, *Inferring periodic orbits from spectra of simply shaped microlasers*, Phys. Rev. A **76**, 023830 (2007).
- [9] N. Sobeshchuk, M. A. Guidry, C. Lafargue, R. Gashemi, D. Decanini, J. Zyss, and M. Lebental, *Out-of-plane modes in three-dimensional Fabry-Perot microlasers*, Appl. Phys. Lett. **112**, 261102 (2018).